Research article

Weixin Liu, Yiming Ma, Yuhua Chang, Bowei Dong, Jingxuan Wei, Zhihao Ren and Chengkuo Lee*

Suspended silicon waveguide platform with subwavelength grating metamaterial cladding for long-wave infrared sensing applications

https://doi.org/10.1515/nanoph-2021-0029
Received January 22, 2021; accepted April 19, 2021;
published online May 7, 2021

Abstract: Long-wave infrared (LWIR, 6–14 μm) processes enormous potential for chem/biosensing as it covers abundant molecular absorption fingerprints. Waveguides provide an attractive chip-scale miniaturization solution for optical sensors. However, the exploration of waveguide sensors in this wavelength range is limited. Here, an LWIR photonic platform for fast and sensitive on-chip gas sensing is developed using suspended silicon (Si) waveguide supported by subwavelength grating (SWG) metamaterial claddings. This platform provides a viable approach to fully exploit the transparency window of Si. The SWG structure provides a promising solution to engineer the mode profile for strong light–analyte interaction. Propagation loss and bending loss are studied in the broad wavelength range of 6.4–6.8 μm. Functional devices including grating couplers, Y-junctions, and directional couplers are also demonstrated with high performance. Sensing demonstration based on our platform is presented using toluene vapor detection as an example. The corresponding limit of detection reaches 75 ppm. The response and recovery time to 75 ppm toluene are about 0.8 and 3.4 s, respectively. This good performance makes our platform a promising candidate for on-site medical and environmental applications.

Keywords: chemical sensor; mid-infrared; photonic platform; subwavelength grating; suspended Si waveguide.

1 Introduction

Numerous photonic solutions have been proposed for chem/biosensing in the midinfrared (MIR) regime, for their label-free analysis capability arising from the unique characteristic spectrum of a given molecular species (a.k.a. molecular fingerprint) [1–10]. Among these, waveguide-based platforms provide an attractive approach for sensor miniaturization and on-chip integration with other components, including microfluidics [11, 12], light sources [13, 14], photodetectors [15, 16], and optoelectronic circuits [17, 18]. Several MIR material platforms have been reported for potential chem/biosensing applications in the last few years [19–21], such as silicon (Si) slot waveguide for ethanol and acetonitrile liquid detection [22], chalcogenide waveguide for methane and nitrous oxide vapor sensing [23], and germanium-on-silicon (GOS) for toluene liquid detection [24]. Silicon-on-insulator (SOI) platform provides another attractive approach for sensing applications, which can leverage the mature complementary metal–oxide–semiconductor (CMOS) fabrication techniques and the abundant infrastructures [25, 26]. However, the severe absorption caused by the buried oxide (BOX) hinders the use of SOI platform for the long-wave infrared (LWIR) wavelength range above 6 μm, which covers the vibrational fingerprints of plentiful chemical bonds including C–H, O–H, N–H, etc. [27, 28]. Fortunately, the subwavelength grating (SWG) assisted suspended Si waveguide has been proved to be a viable solution to solve this problem and can fully exploit the transparency window of Si up to 8 μm [29, 30]. The SWG structure consists of a periodic array of lateral nanobeam, providing both mechanical support for waveguide core and etching access for BOX. Recently, Penades et al. [31] have experimentally demonstrated the feasibility of suspended Si waveguides at the single wavelength of 7.67 μm, with

Weixin Liu and Yiming Ma have contributed equally.

***Corresponding author: Chengkuo Lee**, Department of Electrical and Computer Engineering, National University of Singapore, Singapore, 117583, Singapore; and Center for Intelligent Sensors and MEMS, National University of Singapore, Singapore, 117608, Singapore, E-mail: elelc@nus.edu.sg. https://orcid.org/0000-0002-8886-3649
Weixin Liu, Yiming Ma, Yuhua Chang, Bowei Dong, Jingxuan Wei and Zhihao Ren, Department of Electrical and Computer Engineering, National University of Singapore, Singapore, 117583, Singapore; and Center for Intelligent Sensors and MEMS, National University of Singapore, Singapore, 117608, Singapore

propagation loss of 3.1 ± 0.3 dB/cm. On top of the single wavelength demonstration, it is worthy to investigate the broadband properties of such a platform, because of the importance of fully leveraging its label-free spectroscopic analysis capability. Besides, the development of various functional building blocks is necessary for realization of the photonic sensing system, such as grating couplers for light coupling, Y-junctions, and directional couplers for power spitting, etc.

Limit of detection (LoD) and response time are two key factors of gas/liquid sensors for on-site real-time detections. To date, the typical limits of detection (LoDs) of waveguide platforms are located at several hundred ppm to several tens of thousands ppm [32–37]. The improvement of the sensitivity, and as a result the LoD, is highly desired to meet the requirements of more practical applications. In order to enhance the LoD, several enrich coating layers have been employed for analyte accumulation and sensitivity enhancement of waveguide platforms [38–41], while they usually suffer from slower response times of several tens of seconds, even several tens of minutes. Another approach that does not compromise the response time is to directly enlarge the interaction area between the optical mode and surrounding analyte through waveguide structure design. Several strategies have been reported, including SWG stack waveguides [42, 43], slot waveguides [44], multi-box waveguides [45], etc. The SWG metamaterial claddings in our suspended Si platform can also be employed to enlarge the interaction area while keeping reasonable propagation loss. They provide an engineerable refractive index (RI) of lateral cladding, enabling suspended waveguides with a lower RI contrast in the lateral direction and a higher one in the vertical direction. Therefore, the guided light is vertically well-confined with a large lateral evanescent field ratio for enhancement of the sensitivity. Moreover, the suspended structure further assists in improving the sensitivity and response time because of the additional interaction area underneath waveguides and better mobility of gas flow [36]. Nevertheless, the RI engineering of the SWG metamaterial cladding for sensitivity enhancement has not been well explored yet, in which a trade-off between propagation loss and evanescent field ratio need to be considered.

In this work, an SWG-engineered suspended Si waveguide platform is proposed for LWIR gas sensing applications. The toluene vapor is selected for sensing demonstration as a typical volatile organic compound (VOC), for its massive usage in industries and indicative property for lung cancer [46]. We thoroughly investigate the RI-adjustable property of this platform and its advantages in sensitivity enhancement. Loss performance and mode confinement are studied simultaneously for a reconciliation. The broadband transmission performance of the waveguides is characterized in 6.4–6.8 μm with a propagation loss of 3.9 dB/cm at the absorption fingerprint of toluene (6.65 μm). In addition, broadband characterization of waveguide bends, grating couplers, Y-junctions, and directional couplers are performed in this wavelength range for the first time. Further, an LoD of 75 ppm for toluene detection is experimentally achieved, with the corresponding response and recovery time of only 0.8 and 3.4 s, respectively. The current LoD is mainly limited by the noise floor of our off-chip setup and could be potentially boosted to several ppm level. Our proposed platform can achieve sensitive and super-fast detection, identification, and quantification of a targeted analyte in a gas mixture without additional adsorptive coating, providing many opportunities for on-site applications in environmental monitoring, and clinical diagnosis.

2 Platform concepts

As illustrated in Figure 1A, the proposed LWIR gas detection platform consists of two identical spiral waveguides, a power splitter (Y-junction), and grating couplers, providing simultaneous on-chip sensing, and calibration of analytes. The power splitting function can also be realized by some other building blocks such as multimode interferometer and directional coupler [47, 48]. Two spiral waveguides are separately covered by above-hanging chambers for gas feeding (not shown in the schematic graph). With the sensing waveguide purged with mixture analytes and the reference waveguide purged with atmosphere air, in principle, we can decouple the sensing signal from external influences, including environmental absorption and temperature fluctuation. Thus, this platform provides more robust sensing results, particularly in the low-concentration range. We fabricate the devices from an SOI wafer with a 1.5-μm-thick Si device layer and a 3-μm-thick BOX layer. The device fabrication consists of one-stage lithography and Si deep reactive-ion etching (DRIE) to define the photonic structures, followed by 1:5 hydrogen fluoride etching to locally remove the underneath BOX layer. The inset of Figure 1A shows a cross-sectional scanning electron microscope (SEM) image of the fabricated suspended waveguide, suggesting that the BOX beneath the waveguide is completely removed and the etching sidewalls are vertical and smooth. Figure 1B shows an optical microscope image of the spiral structure characterized in our experiment, with its sensing length L of 28.4 mm. Figure 1C displays the zoom-in graph of the spiral

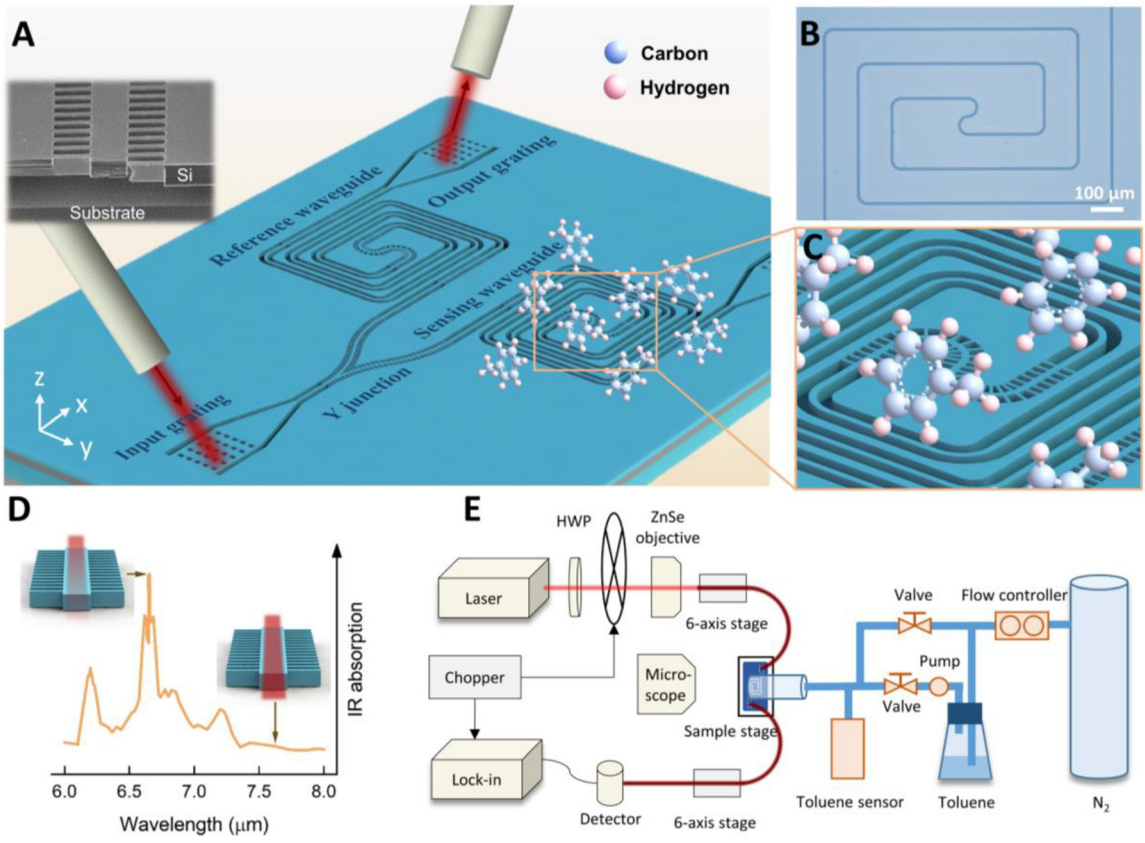

Figure 1: (A) Schematic illustration of the suspended Si waveguide gas sensing platform, consisting of grating couplers, tapers, a power splitter (Y-junction), and spiral waveguides. Inset: cross-sectional scanning electron microscope (SEM) image of the waveguide. (B) Optical image of the suspended Si spiral waveguide. (C) Zoom-in view of the sensing waveguide surrounded by toluene molecules as indicated by the yellow square box in Figure 1A. (D) Absorption spectrum of toluene in 6–8 μm wavelength range. (E) Gas sensing testing setup consisting of an optical characterization module and a gas regulation module. The red lines show the light path (light red: in free space; dark red: in fibers). HWP: half-wave plate.

sensing area. Here, the toluene molecules are uniformly distributed around the waveguide at SWG cladding as well as upper/lower air cladding and interact with the evanescent field of the guided light, resulting in additional absorption. The light transmission intensity will be severely weakened at the characteristic absorption peaks compared with those low-absorption wavelengths, as depicted in Figure 1D, which shows the absorption spectrum of toluene in the range of 6–8 μm and its maximum absorption peak at 6.65 μm wavelength.

The sensing performance of our platform is characterized by the setup depicted in Figure 1E, which can be divided into the optical characterization module and the gas regulation module. In the former module, a continuous-wave quantum cascade laser is employed for light-emitting. A pair of LWIR fibers is used to access the sensing platform through the on-chip grating couplers. The fine alignment between the fibers and the grating couplers is performed with a pair of six-axis alignment stages and a sample stage. Before focused by a ZnSe lens into the input fiber, the light is firstly polarization-controlled by a half-wave plate and modulated by a chopper. The postchip modulated light is converted to an electrical signal by liquid nitrogen cooled MCT detector. This electrical signal is amplified by a pre amplifier before sent to a lock-in amplifier to enhance the signal-to-noise ratio. The optical path is sealed and purged with clean dry air to minimize the optical absorption of ambient environment during the test. In the gas regulation module, nitrogen (N_2) is selected as the buffered gas with its overall flow rate well controlled by a mass flow controller at 2.0 L/min. This buffered gas is divided into two flows, with one pumped into 99.5% toluene solution to generate a toluene-N_2 mixture, and the other remaining as pure N_2. After that, the two flows re-mix, and the toluene concentration in the dilution is calibrated by a commercial sensor before pumped into the gas feeding chamber. The concentration of toluene in the sensing region is precisely and dynamically controlled by regulating

the valves in the two flows, with a wide tuning range from several ppm to several thousand ppm.

3 Device design

The SWG provides a straightforward approach to engineer the effective index, mode profile, and dispersion of the waveguide [49, 50]. In our design, the SWG strips function as metamaterial claddings that provide both lateral light confinement and mechanical support, as the schematic drawing shown in Figure 2A. Here, several factors should be taken into consideration in the waveguide design, including mechanical strength, scattering loss, and mode confinement. In principle, the SWG is optically equivalent to a homogeneous medium with its periodicity shorter than that in the Bragg regime, here achieved by the alternating arrangement of Si strips and air holes. Equivalent RI n_{eff} of the SWG structure is given by [51]:

$$n_{\text{eff}} = \frac{cK}{\omega} \tag{1}$$

$$\begin{aligned}\cos K\Lambda = &\cos(k_1 W_s)\cos(k_2(\Lambda - W_s)) \\ &-\Delta\sin(k_1 W_s)\sin(k_2(\Lambda - W_s))\end{aligned} \tag{2}$$

$$\Delta = \frac{1}{2}\left(\frac{k_2}{k_1} + \frac{k_1}{k_2}\right) \tag{3}$$

$$k_1 = \sqrt{\left(\frac{\omega}{c} n_{\text{Si}}\right)^2 - \beta^2} \tag{4}$$

$$k_2 = \sqrt{\left(\frac{\omega}{c} n_{\text{air}}\right)^2 - \beta^2} \tag{5}$$

Here, $c = 3 \times 10^8$ m/s is the speed of light in vacuum, K is the Bloch wave number, ω is the angular frequency of the electromagnetic (EM) wave determined by the wavelength, W_s is the width of Si nanobeam, and Λ is the SWG period. k_1 and k_2 are the wave vector along the propagation direction, while n_{Si} and n_{air} are the refractive indices of the Si and air, respectively. β represents the projection of the wave vector along the boundary plane, which equals 0 since normal incidence is assumed in our study. Given Eqs. (1)–(5), we notice that n_{eff} is determined by period Λ and duty cycle = W_s/Λ of the SWG structure. Therefore, we study the variation of equivalent RI of SWG as a function of Λ and duty cycle, as depicted in Figure 2B. In general, a larger Λ and duty cycle give higher equivalent RI that assists in sensitivity enhancement of our sensing platform, due to the larger evanescent field ratio of the guided light interacting with target analytes. A further examination is performed to determine the exact value of Λ and duty cycle that realize a low propagation loss, which is desired for longer applicable sensing waveguide length. Finite difference time domain (FDTD) simulation is conducted to extract the propagation loss α of the SWG-engineered waveguide. Here, the waveguide width W_c is fixed at 2.5 μm to provide adequate lateral confinement and minimize the substrate leakage of fundamental quasi transverse electric (TE) mode. The length of SWG beams L_s is chosen as 3 μm to provide sufficient mechanical support while no significant

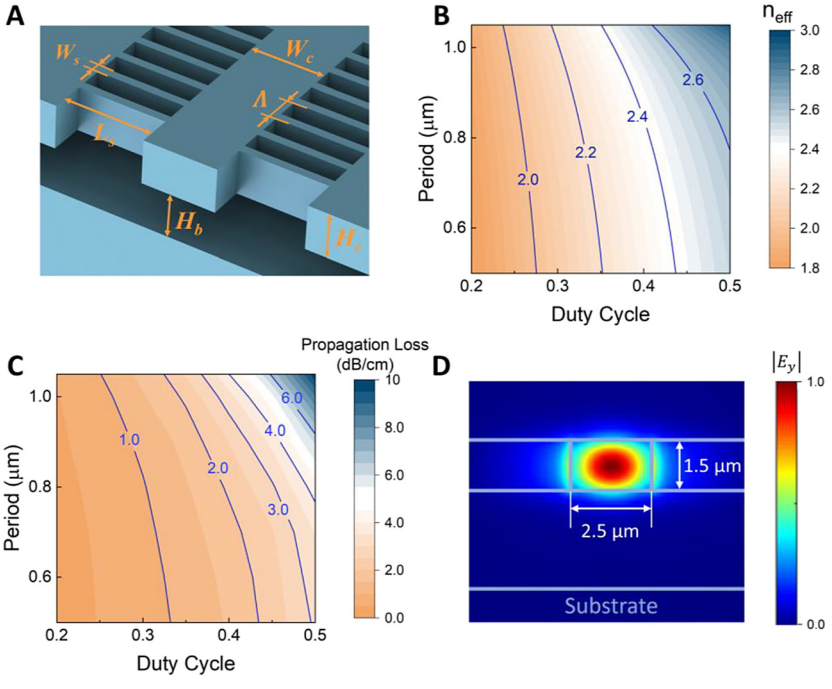

Figure 2: (A) Schematic representation of the suspended waveguide with subwavelength grating (SWG) claddings. (B) SWG equivalent RI n_{eff} and (C) propagation loss of the fundamental quasi transverse electric (TE) mode as a function of SWG period Λ and duty cycle. Waveguide core width and thickness are fixed to be 2.5 and 1.5 μm, respectively. (D) The field distribution of $|E_y|$ for the fundamental quasi-TE mode with the selected SWG period = 1 μm and duty cycle = 0.3.

lateral leakage is introduced. The simulated results are shown in Figure 2C and indicate that larger Λ and duty cycle give a larger loss. The major reason is attributed to the increased lateral scattering resulted from the reduction of RI contract between Si core and the equivalent RI of SWG cladding. Especially, for a given Λ, the propagation loss exhibits an exponential increase along with the duty cycle and vice versa. Thus, the sensitivity of propagation loss with respect to Λ and duty cycle should approach zero to acquire a robust low value of α after taking the fabrication error into consideration. Based on the above discussion, we selected $\Lambda = 1$ μm and $W_s = 0.3$ μm (duty cycle = 0.3). With these values, we achieve a balance between the requirements of a large equivalent RI of SWG ($n_{\text{eff}} = 2.2$) and a low propagation loss ($\alpha = 1.5$ dB/cm) for the high sensitivity of gas sensing. The mode profile of the guided fundamental quasi-TE mode is presented in Figure 2D, with the fundamental quasi transverse magnetic (quasi-TM) mode (>10 dB/cm) and second-order mode (>50 dB/cm) greatly suppressed. Based on this structure, the external confinement factor Γ_{clad} of 24.3% is extracted by simulation. Therefore, the effective sensing length is calculated as $L_{\text{eff}} = \Gamma_{\text{clad}} L = 6.9$ mm (Supplementary material S1).

In order to explore the functionality of our proposed sensing platform, we also design and experimentally investigate the involved components, including grating couplers, 90° bends, power splitters (Y-junctions and directional couplers). Optical images of these building blocks are presented in Figure 3A–D, and the corresponding SEM images of detail structures are showed in Figure 3E–H. Figure 3A and E shows the structure of the designed grating coupler. The effective index contrast herein can be explicitly engineered in two-dimensions to increase the optical bandwidth, alleviate the back reflection, etc. The periodicities of the depicted rectangle holes along the x and y-axis are denoted as P_x and P_y, respectively, while the length and the width of the holes are denoted as G_x and G_y, respectively. Given the optimized parameters ($P_x = 3.9$ μm, $P_y = 3.8$ μm, $G_x = 2.75$ μm, and $G_y = 2.65$ μm) of the grating coupler, an FDTD-simulated maximum coupling efficiency of −5 dB at 6.65 μm with the 1-dB bandwidth of ~210 nm is achieved, while coupled by our LWIR hollow fibers (mode field diameter = 200 μm) with input/output angle of ~10°. Each grating coupler is connected to the waveguide through an adiabatic taper with its width W_t linearly tapered from 40 to 2.5 μm over 700 μm propagation length. The 90° bend is used for straight section connection in our spiral waveguide design, with its bending radius $R_b = 30$ μm as shown in Figure 3B and F. Y-junctions and directional couplers are employed for the power splitting. Y-junctions can divide power into a 50:50 ratio, while directional couplers provide a more flexible approach that splits the power into the desired ratio. Figure 3C and G presents the structure of the cascaded Y-junction with x-span (S_x) of 300 μm and y-span (S_y) of 290 μm. Here, five identical Y-junction structures (outputs labeled as port 1–port 6) are cascaded for extraction of their insertion loss and imbalance. A directional coupler with gap $g = 0.5$ μm is presented in Figure 3D and H, with its critical coupling length $L_c = 45$ μm acquired by the FDTD simulation.

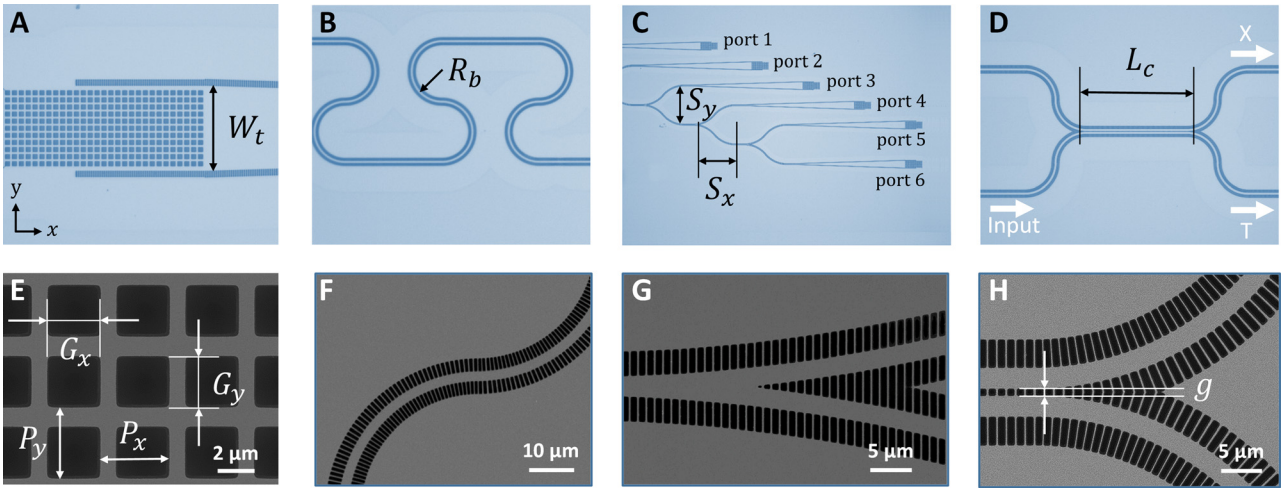

Figure 3: Optical images of (A) Grating coupler; (B) 90° bend waveguide; (C) Cascaded Y-junction; and (D) Directional coupler and their corresponding scanning electron microscope (SEM) images (E)–(H).

4 Results and discussions

Initial characterization of the optical properties is investigated with the optical setup depicted in Figure 1E. To study the broadband performance of our platform, the laser was continuously tuned from 6.4 to 6.8 μm in the experiment. Figure 4A presents the measured and simulated results of the designed grating coupler. The maximum coupling efficiency extracted from the polynomial fitting of the measured data is −7 dB at around 6.63 μm with 1-dB bandwidth of ~170 nm, which is comparable with those of reported MIR grating couplers (Supplementary material S2). It is worth noting that the measured spectra are well-matched with the simulated results, while the latter predicts ~2 dB higher maximum efficiency located at ~6.65 μm with 1-dB bandwidth of ~210 nm. A cutback method is employed to extract the propagation loss and bending loss of our suspended Si platform. Figure 4B shows a relatively flat propagation loss spectrum across the measured wavelength range with an average of 4.3 dB/cm and a standard deviation of 0.39 dB/cm. The inset of Figure 4B shows the representative cutback measurement results at the absorption peak of toluene vapor (6.65 μm), where the slope of the linear fitting reveals the propagation loss of 3.9 dB/cm. The bending loss is depicted in Figure 4C, which shows only ~0.06 dB per bend with a radius of 30 μm. The cutback results at 6.65 μm are presented in the inset of Figure 4C as well. The measured propagation and bending losses are also comparable with those of reported MIR waveguide platforms (Supplementary material S3).

The power-splitting performance of Y-junctions and directional couplers are also studied through the experiment. Figure 5A presents the transmission result of the cascaded Y-junction measured from different ports as labeled in Figure 3C. The slopes extracted from linear fitting show insertion loss of −0.43 ± 0.18, −0.09 ± 0.11, −0.10 ± 0.10, and −0.03 ± 0.25 dB at 6.56, 6.59, 6.62, and 6.65 μm, respectively. Figure 5B shows the power imbalance of our Y-junction across the depicted wavelengths, which is extracted from the transmission of port 5 and port 6 shown in the inset optical image. The experimental results confirm a broadband 50:50 power splitting ratio with low insertion loss and low imbalance, suggesting the Y-junction as a liable approach for equal distribution of light intensity. Another proposed power splitter is the directional coupler that gives an adjustable power splitting ratio between two output ports. Here we characterize a directional coupler with its gap $g = 0.5$ μm. The relationship between the coupling length L_c and the self-normalized transmission in the transmitted port (T/I) and coupled port (X/I) at 6.65 μm is depicted in Figure 5C, where T and X are the power measured at the transmitted port and coupled port, respectively (see Figure 3D). $I = X + T$ is the total power of the above two ports. According to the coupled-mode theory, the data are fitted with a sine-squared function [52]. An adjusted R-square of 0.994 is obtained, showing a good agreement between the measured data and the theoretical prediction. To further visualize the broadband performance of the directional coupler, we plot the dependence of power coupling efficiency K on both wavelength and L_c simultaneously to get the color contour map as presented in Figure 5D. At the wavelength range of 6.45–6.7 μm, different coupling efficiencies could be achieved in directional couplers with suitable L_c. This contour map serves as a design guideline for the directional coupler with desired power splitting ratio.

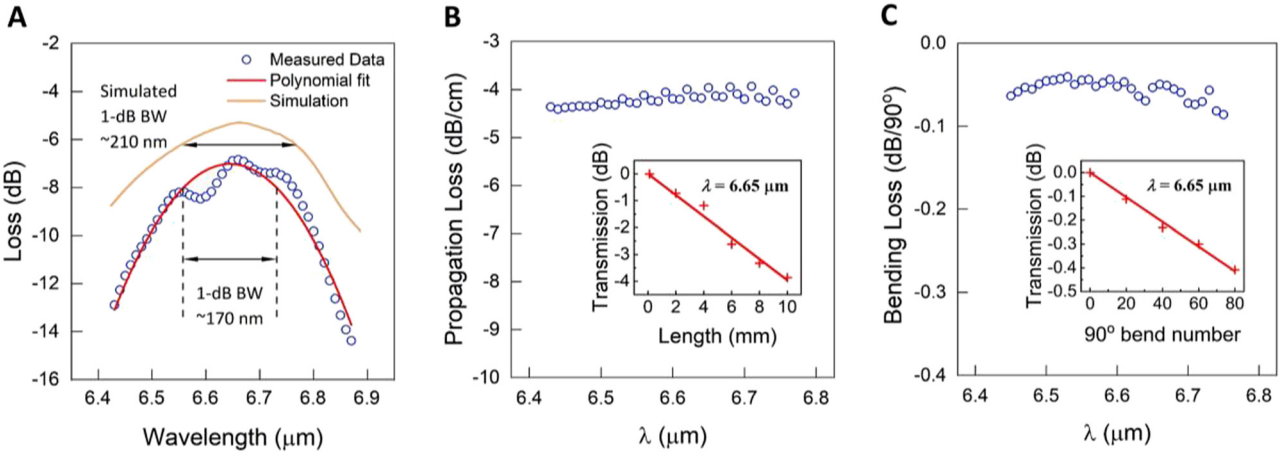

Figure 4: Optical characterization.
(A) Simulated and measured coupling efficiency and 1-dB bandwidth of the grating coupler. (B) Propagation loss. Inset: cutback results measured at 6.65 μm; (C) 90° bending loss. Inset: cutback results at 6.65 μm.

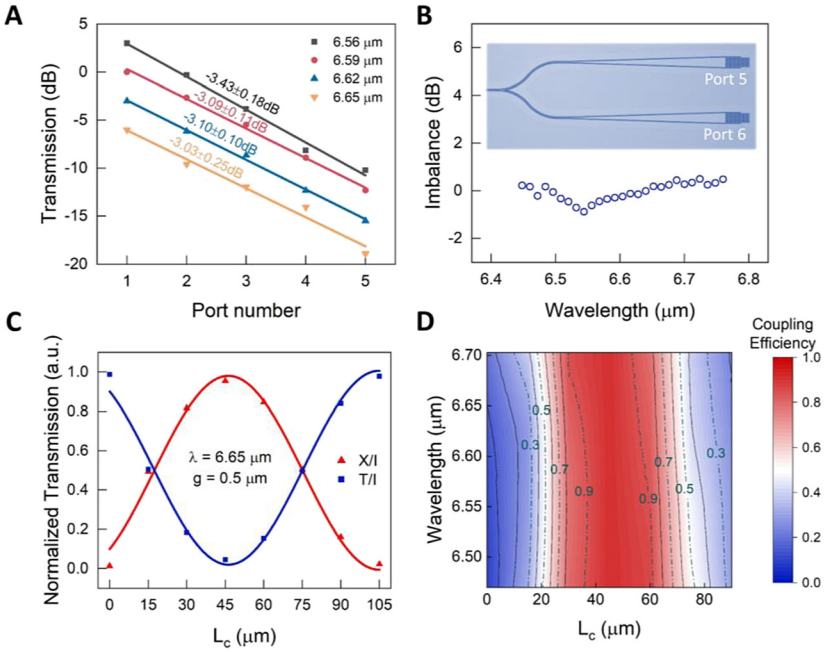

Figure 5: Device characterization. (A) Cutback results of the cascaded Y-junction at 6.56, 6.59, 6,62, and 6.65 μm. (B) The power imbalance of the Y-junction. Inset: optical image of port 5 and port 6 of the cascaded Y-junction where the result is measured. (C) Self-normalized transmitted (T/I) and coupled (X/I) powers of the directional coupler with g = 0.5 μm at 6.65 μm. (D) Contour map of the dependence of K on L_c and wavelength for the directional coupler.

Toluene vapor was chosen to examine the sensing capability of our platform. As mentioned earlier, the concentration of toluene in the sensing area is precisely controlled by the adjustable valves in two gas flows and calibrated by a commercial sensor. To characterize the absorbance under certain toluene concentrations, we alternately injected nitrogen (N_2) and toluene-N_2 dilutions. Figure 6A shows the testing results of the toluene absorbance at 6.65 μm versus toluene concentration ranging from 144 to 1114 ppm. The absorbance is calculated based on the average transmission change in three response and recovery characterization cycles. A linear fit is employed to the measured data, and a sensitivity of 2.8×10^{-5}/ppm is extracted. The R-square of the fitting result is 0.995, showing a good linear response behavior. To further explore the LoD of our platform, absorbance responses to alternate injection between pure N_2 and 75 ppm toluene-N_2 dilutions are presented in Figure 6B. The results experimentally show an LoD down to 75 ppm, which is limited by the off-chip noise floor and leaves a large room for

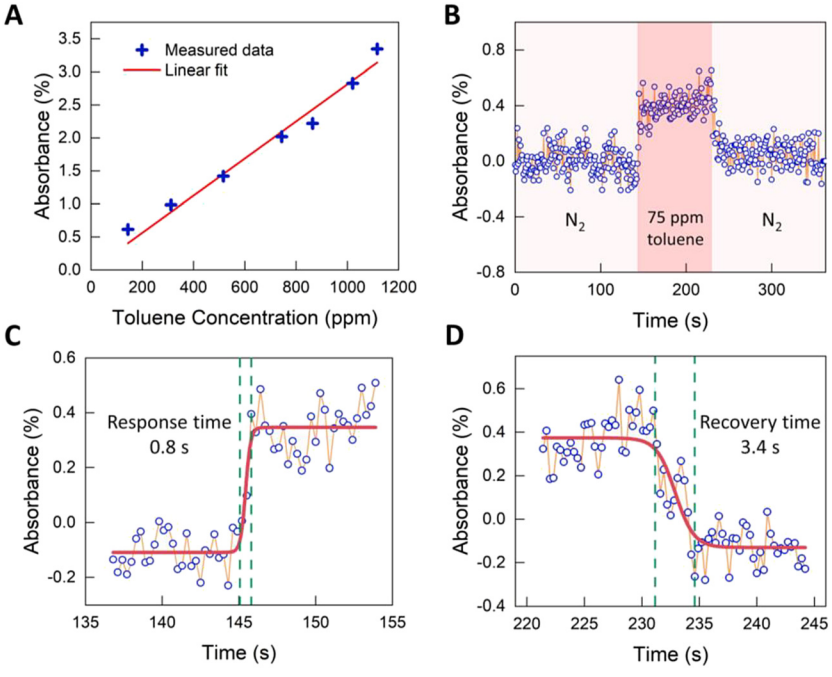

Figure 6: (A) Optical absorbance of toluene at its absorption peak of 6.65 μm versus toluene concentration. The red line is a linear fitting to the measured data. (B) Response and recovery characteristic cycle curves of the suspended silicon (Si) platform to alternative injection between pure N_2 and 75 ppm toluene-N_2 dilution. (C) Response time. (D) Recovery time.

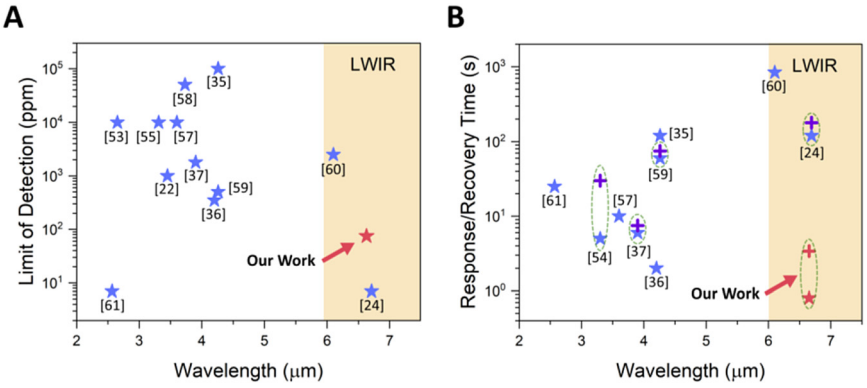

Figure 7: Comparison of reported absorption-based waveguide sensors on (A) Limit of detection and (B) response/recovery time. Our results are indicated in red. In (B), response times are indicated by stars, and recovery times are indicated by crosses.

improvement. Figure 6C and D show the response and recovery stage extracted from Figure 6B, respectively, which are fitted with Boltzmann curves and indicate a response time of 0.8 s and a recovery time of 3.4 s with regard to 75 ppm toluene detection. It is verified that the flow rate is fast enough and has negligible influence on the response and recovery times (Supplementary material S4). The temporally asymmetric behavior of our platform could be explained by the dynamic interaction between the analyte and the waveguides. More specifically, as toluene is in the liquid phase at room temperature, it is unavoidable that a fraction of the vapor will condense into fine droplets on the surface of waveguides. The liquid–solid interaction between two materials is rather strong due to the large surface free energy of Si [62]. This makes the absorption of toluene easier than desorption, and as a result, a longer recovery time than the response time. Despite this, the response/recovery time of our sensor is still fast enough for real-time on-site monitoring applications.

In Figure 7A and B, we compare our results with those of other reported MIR absorption-based waveguide sensors [22, 24, 35–37, 53–61]. Our platform features an outstanding performance on LoD and response time amongst all the listed works. We note Ref. [24] estimated an LoD of 7 ppm for toluene detection at the LWIR range as well (Figure 7A), which is mainly attributed to the accumulative effect of applied mesoporous silica coating (concentration enhancement factors up to 760). However, due to the same reason, the response time of their platform is ~2 min, much slower than what we achieved (Figure 7B). Our platform presents a low LoD and a fast response time simultaneously, thanks to the well-designed SWG and suspended structure, and high-quality fabrication process. Moreover, by optimizing the scattering loss and employing a low-noise light source, we can further reduce the LoD of our platform to several ppm (Supplementary material S5) [24, 63, 64].

5 Conclusion

In conclusion, a suspended Si waveguide platform with SWG claddings is proposed for sensitive and fast chip-scale integrated chemical sensing in the LWIR range, and its sensing performance of toluene vapor is investigated. A flat propagation loss spectrum of ~4.3 dB/cm is measured across a broad wavelength range of 6.4–6.8 μm. Various functional devices, including grating couplers, Y-junctions, and directional couplers, are demonstrated with high performance. The engineerable equivalent RI of the SWG claddings provides a promising and flexible approach for sensitivity enhancement. An LoD of 75 ppm for toluene vapor sensing is experimentally achieved, with the corresponding response and recovery time of 0.8 and 3.4 s, respectively. With further optimization of the losses and reduction of the noise floor by using a high-power and low-noise light source, a lower LoD down to several ppm is expected. The demonstrated good performance and the cost-effective CMOS fabrication process endow our platform with enormous potential for many real-time environmental and medical applications.

Author contribution: All the authors have accepted responsibility for the entire content of this submitted manuscript and approved submission.
Research funding: This work was supported by NRF-CRP15-2015-02 “Piezoelectric Photonics Using CMOS Compatible AlN Technology for Enabling the Next Generation Photonics ICs and Nanosensors” and NRF-ISF Joint Research Grant (NRF2015-NRF-ISF001-2620) “Reconfigurable data center optical interconnects using fast nanophotonic MEMS waveguide switches” at National University of Singapore, Singapore.
Conflict of interest statement: The authors declare no conflicts of interest regarding this article.

References

[1] H. Zhou, X. Hui, D. Li, et al., "Metal-organic framework-surface-enhanced infrared absorption platform enables simultaneous on-chip sensing of greenhouse gases," *Adv. Sci.*, vol. 7, p. 2001173, 2020.

[2] Y. Chen, W. S. Fegadolli, W. M. Jones, A. Scherer, and M. Li, "Ultrasensitive gas-phase chemical sensing based on functionalized photonic crystal nanobeam cavities," *ACS Nano*, vol. 8, pp. 522–527, 2014.

[3] Y. Chang, J. Wei, and C. Lee, "Metamaterials – from fundamentals and MEMS tuning mechanisms to applications," *Nanophotonics*, vol. 9, pp. 3049–3070, 2020.

[4] H. Lin, Y. Song, Y. Huang, et al., "Chalcogenide glass-on-graphene photonics," *Nat. Photonics*, vol. 11, pp. 798–805, 2017.

[5] V. Mittal, M. Nedeljkovic, D. J. Rowe, G. S. Murugan, and J. S. Wilkinson, "Chalcogenide glass waveguides with paper-based fluidics for mid-infrared absorption spectroscopy," *Opt. Lett.*, vol. 43, pp. 2913–2916, 2018.

[6] Z. Ren, Y. Chang, Y. Ma, K. Shih, B. Dong, and C. Lee, "Leveraging of MEMS technologies for optical metamaterials applications," *Adv. Opt. Mater.*, vol. 8, p. 1900653, 2019.

[7] V. Mittal, G. Devitt, M. Nedeljkovic, et al., "Ge on Si waveguide mid-infrared absorption spectroscopy of proteins and their aggregates," *Biomed. Opt. Express*, vol. 11, pp. 4714–4722, 2020.

[8] Y. S. Lin and Z. Xu, "Reconfigurable metamaterials for optoelectronic applications," *Int. J. Optomechatronics*, vol. 14, pp. 78–93, 2020.

[9] B. Dong, X. Luo, S. Zhu, et al., "Aluminum nitride on insulator (AlNOI) platform for mid-infrared photonics," *Opt. Lett.*, vol. 44, pp. 73–76, 2019.

[10] V. Vakarin, J. M. Ramírez, J. Frigerio, et al., "Ultra-wideband Ge-rich silicon germanium integrated Mach–Zehnder interferometer for mid-infrared spectroscopy," *Opt. Lett.*, vol. 42, pp. 3482–3485, 2017.

[11] J. Xu, Y. Du, Y. Tian, and C. Wang, "Progress in wafer bonding technology towards MEMS, high-power electronics, optoelectronics, and optofluidics," *Int. J. Optomechatronics*, vol. 14, pp. 94–118, 2020.

[12] J. Xu, Z. Ren, B. Dong, et al., "Nanometer-scale heterogeneous interfacial sapphire wafer bonding for enabling plasmonic-enhanced nanofluidic mid-infrared spectroscopy," *ACS Nano*, vol. 14, pp. 12159–12172, 2020.

[13] H. Lin, Z. Luo, T. Gu, et al., "Mid-infrared integrated photonics on silicon: a perspective," *Nanophotonics*, vol. 7, pp. 393–420, 2018.

[14] J. Wei, Z. Ren, and C. Lee, "Metamaterial technologies for miniaturized infrared spectroscopy: light sources, sensors, filters, detectors, and integration," *J. Appl. Phys.*, vol. 128, p. 240901, 2020.

[15] Y. Ma, B. Dong, J. Wei, et al., "High-responsivity mid-infrared black phosphorus slow light waveguide photodetector," *Adv. Opt. Mater.*, vol. 8, p. 2000337, 2020.

[16] J. Wei, Y. Li, L. Wang, et al., "Zero-bias mid-infrared graphene photodetectors with bulk photoresponse and calibration-free polarization detection," *Nat. Commun.*, vol. 11, p. 6404, 2020.

[17] B. Dong, Y. Yang, Q. Shi, et al., "Wearable triboelectric-human-machine interface (THMI) using robust nanophotonic readout," *ACS Nano*, vol. 14, pp. 8915–8930, 2020.

[18] B. Dong, Q. Shi, T. He, et al., "Wearable triboelectric/aluminum nitride nano-energy-nano-system with self-sustainable photonic modulation and continuous force sensing," *Adv. Sci.*, vol. 7, p. 1903636, 2020.

[19] J. Amirez, V. L. V. Akarin, C. L. G. Illes, et al., "Low-loss Ge-rich $Si_{0.2}$ $Ge_{0.8}$ waveguides for mid-infrared photonics," *Opt. Lett.*, vol. 42, pp. 105–108, 2017.

[20] Y. Chen, H. Lin, J. Hu, and M. Li, "Heterogeneously integrated silicon photonics for the mid-infrared and spectroscopic sensing," *ACS Nano*, vol. 8, pp. 6955–6961, 2014.

[21] T. Jin, J. Zhou, H. Y. G. Lin, and P. T. Lin, "Mid-infrared chalcogenide waveguides for real-time and nondestructive volatile organic compound detection," *Anal. Chem.*, vol. 91, pp. 817–822, 2019.

[22] P. T. Lin, S. W. Kwok, H. Y. G. Lin, et al., "Mid-infrared spectrometer using opto-nanofluidic slot-waveguide for label-free on-chip chemical sensing," *Nano Lett.*, vol. 14, pp. 231–238, 2014.

[23] A. Gutierrez-Arroyo, E. Baudet, L. Bodiou, et al., "Optical characterization at 7.7 μm of an integrated platform based on chalcogenide waveguides for sensing applications in the mid-infrared," *Opt. Express*, vol. 24, pp. 23109–23117, 2016.

[24] N. T. Benéitez, B. Baumgartner, J. Missinne, et al., "Mid-IR sensing platform for trace analysis in aqueous solutions based on a germanium-on-silicon waveguide chip with a mesoporous silica coating for analyte enrichment," *Opt. Express*, vol. 28, pp. 27013–27027, 2020.

[25] T. Hu, B. Dong, X. Luo, et al., "Silicon photonic platforms for mid-infrared applications," *Photonics Res.*, vol. 5, pp. 417–30, 2017.

[26] Y. Chang, B. Dong, Y. Ma, J. Wei, Z. Ren, and C. Lee, "Vernier effect-based tunable mid-infrared sensor using silicon-on-insulator cascaded rings," *Opt. Express*, vol. 28, pp. 6251–6260, 2020.

[27] Y. Ma, B. Dong, B. Li, K-W. Ang, and C. Lee, "Dispersion engineering and thermo-optic tuning in mid-infrared photonic crystal slow light waveguides on silicon-on-insulator," *Opt. Lett.*, vol. 43, pp. 5504–5507, 2018.

[28] D. A. Kozak, T. H. Stievater, R. Mahon, and W. S. Rabinovich, "Germanium-on-silicon waveguides at wavelengths from 6.85 to 11.25 microns," *IEEE J. Sel. Top. Quant. Electron.*, vol. 24, pp. 6–9, 2018.

[29] J. S. Penades, A. Ortega-Moñux, M. Nedeljkovic, et al., "Suspended silicon mid-infrared waveguide devices with subwavelength grating metamaterial cladding," *Opt. Express*, vol. 24, pp. 22908–22916, 2016.

[30] J. Soler Penadés, C. Alonso-Ramos, A. Z. Khokhar, et al., "Suspended SOI waveguide with sub-wavelength grating cladding for mid-infrared," *Opt. Lett.*, vol. 39, pp. 5661–5664, 2014.

[31] J. S. Penadés, A. Sánchez-Postigo, M. Nedeljkovic, et al., "Suspended silicon waveguides for long-wave infrared wavelengths," *Opt. Lett.*, vol. 43, pp. 795–798, 2018.

[32] C. J. Smith, R. Shankar, M. Laderer, M. B. Frish, M. Loncar, and M. G. Allen, "Sensing nitrous oxide with QCL-coupled silicon-on-sapphire ring resonators," *Opt. Express*, vol. 23, pp. 5491–5499, 2015.

[33] Y. Ma, B. Dong, and C. Lee, "Progress of infrared guided-wave nanophotonic sensors and devices," *Nano Converg.*, vol. 7, p. 12, 2020.

[34] C. Ranacher, C. Consani, A. Tortschanoff, et al., "Mid-infrared absorption gas sensing using a silicon strip waveguide," *Sens. Actuators A*, vol. 277, pp. 117–123, 2018.
[35] C. Consani, C. Ranacher, A. Tortschanoff, T. Grille, P. Irsigler, and B. Jakoby, "Mid-infrared photonic gas sensing using a silicon waveguide and an integrated emitter," *Sens. Actuators B Chem.*, vol. 274, pp. 60–65, 2018.
[36] F. Ottonello-Briano, C. Errando-Herranz, H. Rödjegård, H. Martin, H. Sohlström, and K. B. Gylfason, "Carbon dioxide absorption spectroscopy with a mid-infrared silicon photonic waveguide," *Opt. Lett.*, vol. 45, pp. 109–112, 2020.
[37] M. S. Yazici, B. Dong, D. Hasan, F. Sun, and C. Lee, "Integration of MEMS IR detectors with MIR waveguides for sensing applications," *Opt. Express*, vol. 28, pp. 11524–11537, 2020.
[38] H. Zhao, B. Baumgartner, A. Raza, A. Skirtach, B. Lendl, and R. Baets, "Multiplex volatile organic compound Raman sensing with nanophotonic slot waveguides functionalized with a mesoporous enrichment layer," *Opt. Lett.*, vol. 45, pp. 447–450, 2020.
[39] G. Antonacci, J. Goyvaerts, H. Zhao, B. Baumgartner, B. Lendl, and R. Baets, "Ultra-sensitive refractive index gas sensor with functionalized silicon nitride photonic circuits," *APL Photonics*, vol. 5, p. 081301, 2020.
[40] Z. Zhang, X. Zhang, T. Rajh, and S. Guha, "Photonic microresonator based sensor for selective nitrate ion detection," *Sens. Actuators B Chem.*, vol. 328, p. 129027, 2021.
[41] G. Tuerdi, N. Kari, Y. Yan, P. Nizamidin, and A. Yimit, "A functionalized tetrakis (4-nitrophenyl) porphyrin film optical waveguide sensor for detection of H_2S and ethanediamine gases," *Sensors*, vol. 17, p. 2717, 2017.
[42] H. Yan, L. Huang, X. Xu, et al., "Unique surface sensing property and enhanced sensitivity in microring resonator biosensors based on subwavelength grating waveguides," *Opt. Express*, vol. 24, pp. 29724–29733, 2016.
[43] C. W. Chang, X. Xu, S. Chakravarty, et al., "Pedestal subwavelength grating metamaterial waveguide ring resonator for ultra-sensitive label-free biosensing," *Biosens. Bioelectron.*, vol. 141, p. 111396, 2019.
[44] W-C. Lai, S. Chakravarty, X. Wang, C. Lin, and R. T. Chen, "On-chip methane sensing by near-IR absorption signatures in a photonic crystal slot waveguide," *Opt. Lett.*, vol. 36, pp. 984–986, 2011.
[45] E. Luan, H. Yun, L. Laplatine, et al., "Enhanced sensitivity of subwavelength multibox waveguide microring resonator label-free biosensors," *IEEE J. Sel. Top. Quant. Electron.*, vol. 25, p. 7300211, 2019.
[46] G. Peng, U. Tisch, O. Adams, et al., "Diagnosing lung cancer in exhaled breath using gold nanoparticles," *Nat. Nanotechnol.*, vol. 4, pp. 669–673, 2009.
[47] B. Dong, X. Luo, S. Zhu, et al., "Thermal annealing study of the mid-infrared aluminum nitride on insulator (AlNOI) photonics platform," *Opt. Express*, vol. 22, pp. 19815–19826, 2019.
[48] B. Dong, T. Hu, X. Luo, et al., "Wavelength-flattened directional coupler based mid-infrared chemical sensor using Bragg wavelength in subwavelength grating structure," *Nanomaterials*, vol. 8, p. 893, 2018.
[49] P. J. Bock, P. Cheben, J. H. Schmid, et al., "Subwavelength grating periodic structures in silicon-on-insulator: a new type of microphotonic waveguide," *Opt. Express*, vol. 18, pp. 20251–20262, 2010.
[50] P. Cheben, R. Halir, J. H. Schmid, H. A. Atwater, and D. R. Smith, "Subwavelength integrated photonics," *Nature*, vol. 560, pp. 565–572, 2018.
[51] P. Yeh, A. Yariv, and C. S. Hong, "Electromagnetic propagation in periodic stratified media. I. General theory," *J. Opt. Soc. Am.*, vol. 67, pp. 438–448, 1977.
[52] A. Hardy and W. Streifer, "Coupled mode theory of parallel waveguides," *J. Light Technol.*, vol. 3, pp. 1135–1146, 1985.
[53] T. Jin, H. Y. G. Lin, T. Tiwald, and P. T. Lin, "Flexible mid-infrared photonic circuits for real-time and label-free hydroxyl compound detection," *Sci. Rep.*, vol. 9, p. 4153, 2019.
[54] P. T. Lin, V. Singh, J. Hu, et al., "Chip-scale mid-infrared chemical sensors using air-clad pedestal silicon waveguides," *Lab Chip*, vol. 11, pp. 2161–2166, 2013.
[55] P. Su, Z. Han, D. Kita, et al., "Monolithic on-chip mid-IR methane gas sensor with waveguide-integrated detector," *Appl. Phys. Lett.*, vol. 114, p. 051103, 2019.
[56] M. Malmström, M. Karlsson, P. Forsberg, Y. Cai, F. Nikolajeff, and F. Laurell, "Waveguides in polycrystalline diamond for mid-IR sensing," *Opt. Mater. Express*, vol. 6, pp. 1286–1295, 2016.
[57] P. T. Lin, H. Y. G. Lin, Z. Han, et al., "Label-free glucose sensing using chip-scale mid-infrared integrated photonics," *Adv. Opt. Mater.*, vol. 4, pp. 1755–1759, 2016.
[58] W. Li, P. Anantha, K. H. Lee, et al., "Spiral waveguides on germanium-on-silicon nitride platform for mid-IR sensing applications," *IEEE Photonics J.*, vol. 10, p. 2201107, 2018.
[59] C. Ranacher, C. Consani, N. Vollert, et al., "Characterization of evanescent field gas sensor structures based on silicon photonics," *IEEE Photonics J.*, vol. 10, p. 2700614, 2018.
[60] V. Mittal, M. Nedeljkovic, L. G. Carpenter, et al., "Waveguide absorption spectroscopy of bovine serum albumin in the mid-infrared fingerprint region," *ACS Sens.*, vol. 4, pp. 1749–1753, 2019.
[61] M. Vlk, A. Datta, S. Alberti, et al., "Extraordinary evanescent field confinement waveguide sensor for mid-infrared trace gas spectroscopy," *Light Sci. Appl.*, vol. 10, p. 26, 2021.
[62] E. J. Chibowski, "Surface free energy and wettability of silyl layers on silicon determined from contact angle hysteresis," *Adv. Colloid Interface Sci.*, vol. 113, pp. 121–131, 2005.
[63] Z. Han, P. Lin, V. Singh, et al., "On-chip mid-infrared gas detection using chalcogenide glass waveguide," *Appl. Phys. Lett.*, vol. 108, p. 141106, 2016.
[64] A. Schwaighofer, M. Montemurro, S. Freitag, C. Kristament, M. J. Culzoni, and B. Lendl, "Beyond Fourier transform infrared spectroscopy: external cavity quantum cascade laser-based mid-infrared transmission spectroscopy of proteins in the amide I and amide II region," *Anal. Chem.*, vol. 90, pp. 7072–7079, 2018.

Supplementary Material: The online version of this article offers supplementary material (https://doi.org/10.1515/nanoph-2021-0029).